Design and Experiment for Dual-Mass MEMS Gyroscope Sensing Closed-Loop System

**HUILIANG CAO, (Member, IEEE), RIHUI XUE, QI CAI, JINYANG GAO, RUI ZHAO,
YUNBO SHI, KUN HUANG, XINGLING SHAO, AND CHONG SHEN**
Science and Technology on Electronic Test & Measurement Laboratory, North University of China, Taiyuan 030051, China

Corresponding authors: Xingling Shao (shaoxl@nuc.edu.cn) and Chong Shen (shenchong@nuc.edu.cn)

ABSTRACT A closed-loop controlling system for Micro Electro Mechanical System (MEMS) gyroscope sense mode is investigated in this paper, and the controller is designed to achieve low error, wide bandwidth and low noise capability. The gyroscope monitoring system includes four independent closed-loop, and is simulated by Simulink soft to prove the speedability and stability of the sensing closed-loop. The gyroscope monitoring system is realized through 3 analog circuit boards, and is tested through temperature controlled turntable. The bias stability, angular random walking value and bias temperature coefficients improved from 2.168 °/h, 0.155°/√h and 10.59 °/h/°C to 0.415 °/h, 0.0414°/√h and 3.59°/h/°C. And the bandwidth value is improved from 13Hz to 104Hz. Meanwhile, scale factor nonlinearity, asymmetry, repeatability and temperature coefficient parameters are enhanced from 660 ppm, 430ppm, 403ppm and 180 ppm/°C to 59.3ppm, 62.4ppm, 50.4ppm and 28.7 ppm/°C respectively.

INDEX TERMS Micro Electro Mechanical System (MEMS) gyroscope, sensing closed-loop, experiment, quadrature error, step response.

I. INTRODUCTION

With the development of MEMS relative technology, new technology and devices are applied in civil and military fields, such as including micro robot, energy harvesting, automotive safety, aircraft and vehicle control, attitude determination, industrial controlling, inertial navigation, micro signal detection, equipment fault diagnosis and consumer electronics [1]–[11]. And MEMS gyroscope is one of the most important representative of MEMS device that require multi discipline and technology, including structure optimization [12], weak signal detection [13], [14], output signal drift analysis [15], structure mechanical model analysis [16]–[18], output data temperature compensation [19]–[21], quadrature error compensation [22], and so

The associate editor coordinating the review of this manuscript and approving it for publication was Quinn Qiao.

on. Sensing closed-loop can improve the characteristic of gyroscope. In work [23]–[27], traditional PI controller was employed in gyroscope sensing closed-loop, and outstanding results were achieved: the gyroscope bias stability is better than 0.1°/h [23] and 3°/h [24], and the controllers were reported to have excellent temperature subject range (−25°C to 70°C in [23] and −40°C to 125°C in [24]). Furthermore, the sensing closed loop improves the scale factor [25], bandwidth [16], [17], [27] and anti vibration [26] performance of gyroscope. Genetic algorithm was employed in reference [28] and [29] to form the sensing closed-loop, and with the help of sigma-delta modulator, the system achieves better performance than sensing open loop. Work [30] proposed a novel decentralized sense mode closed-loop, and MEMS gyroscope bias stability characteristic enhanced a lot. And, in work [31] and [32], sigma-delta modulator in sensing closed-loop improves the noise characteristic of the gyroscope. Paper
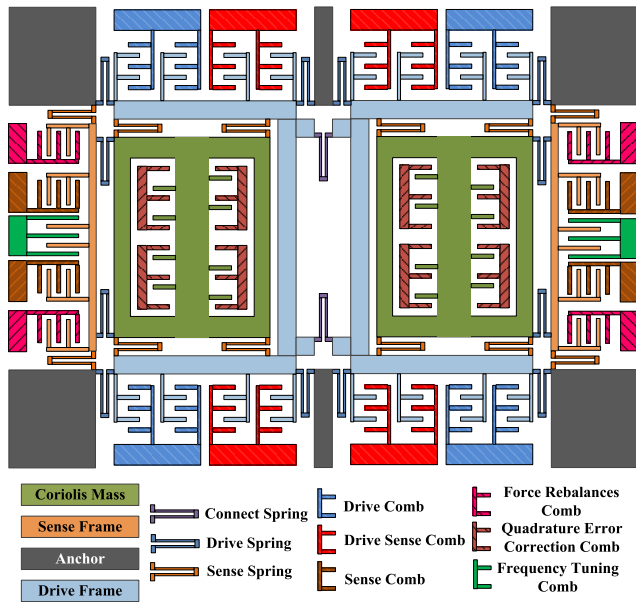
FIGURE 1. The structure diagram of dual-mass MEMS gyroscope investigated in this paper.

[33] utilized automatic gain controlling (AGC) method to control the sensing mode of a single mass gyroscope. Work [34] investigated the notch filter technology in sense mode close-loop, and the scale factor characteristic and bandwidth were better than sensing open-loop. A narrow-band controller was utilized in sense mode feedback loop in reference [35], and improves some dynamic parameters of gyroscope. Work [36] reported a sensing closed-loop controlling method by employing fuzzy reliability and Taguchi design technology, which enhanced the temperature performance of the gyroscope.

The aim of this paper is to investigate the MEMS gyroscope sensing closed-loop, and also, the controller is supposed to simple, and have better temperature adaption. With the sensing closed-loop, the gyroscope performance will be improved obviously. The rest of the paper is organized as: Section II introduces the MEMS gyroscope structure including mode analysis and equation of motion. In Section III, sensing closed-loop is designed based on Sensing closed-loop Controller (SCLC), and the system is analyzed and simulated. Then, in Section IV, the gyroscope sensing open-loop together with the closed-loop systems are tested and the SCLC system results are shown. Finally, in Section V, the test results are discussed and the conclusion is remarked.

II. MEMS GYROSCOPE SENSITIVITY STRUCTURE

The MEMS gyroscope structure diagram investigated in this paper is shown in Figure. 1 [7], [8].

From Fig.1 it can be seen that the structure is symmetrical and is divided into left and right part. And two connect springs link the left and part together. For left or right part, the structure can be divided as one "U" shaped drive frame, one sense frame, six drive springs, six sense springs, one Coriolis mass
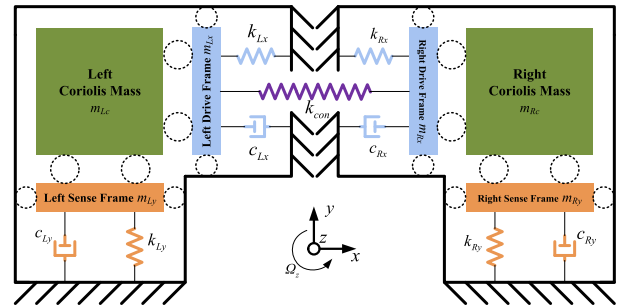

FIGURE 2. The mechanical diagram of dual-mass MEMS gyroscope structure.

and one group of drive comb, drive sense comb, sense comb, force rebalances comb, quadrature error correction comb and frequency tuning comb. The whole structure has six anchor, which was bonded to glass basement, and the springs, frames and Coriolis mass are impending and supported by anchors. The "U" shaped springs can release the thermal stress during the bonding process.

The structure equivalent mechanical model is shown in Fig. 2, the left and right mechanical system is connected by connect spring (with the stiffness coefficient as k_{con}). And it is obviously that the structure is typical decoupled one, which is better for signal detection and coupled error suppression.

The frequency tuning comb is based on squeeze film type, which can provide electrostatic negative stiffness and change the sense mode resonant frequency to optimize the mechanical sensitivity and bandwidth. The quadrature error correction comb employed non equal distance squeeze film type, which can generate electrostatic negative stiffness to correct the quadrature coupling stiffness [22]. Other combs are slide film type, and the linearity is better and different combs have their own functions: Drive comb is used to stimulate the drive mode of the gyroscope; Drive sense comb is utilized to detect the amplitude of drive mode; Sense comb is employed to pick up the movement of sense mode; Force rebalances comb is used to generate the sense feedback force.

The first eight order modes of the structure are simulated and shown in Fig. 3, and the working modes should be emphasized. The sensing in-phase mode (Q value is Q_{y1}, and resonant frequency is ω_{y1}) is shown in Fig. 3 (b), and two Coriolis masses move along y axis in same direction. The 3rd mode is sensing anti-phase mode (which is shown in Fig. 3(c) with resonant frequency ω_{y2} and Q value is Q_{y2}), two Coriolis masses vibrate in inverse direction along y axis. The drive anti-phase mode is shown in Fig. 3 (d), with resonant frequency ω_x and in this mode, two Coriolis masses move in inverse direction along x axis.

The left and right gyroscope mechanical systems are independent and their motion equation can be expressed as [7]:

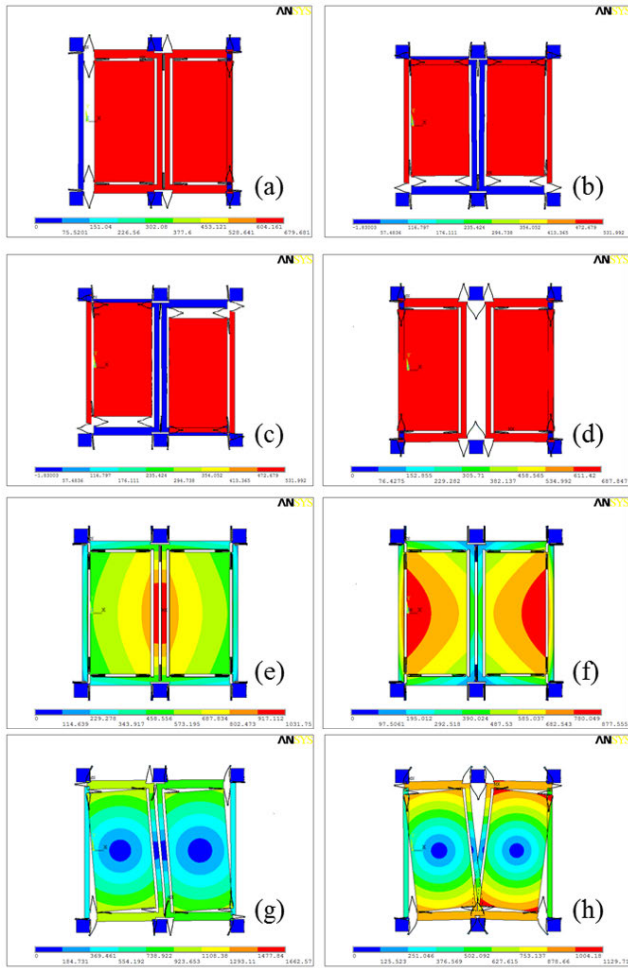$$m\ddot{D} + \omega m \frac{1}{Q}\dot{D} + m\omega^2 D = F \qquad (1)$$

FIGURE 3. MEMS gyroscope structure lower eight vibration order: (a) Drive in-phase mode (16481rad/s); (b) Sensing in-phase mode(20998 rad/s); (c) Sensing anti-phase mode(21790 rad/s); (d) Drive anti phase mode(21891 rad/s); (e) Z axis out plane mode(25981 rad/s); (f) structure Z axis shape change mode (30316 rad/s); (g) Z axis in phase twist mode(39741 rad/s); (h) Z axis anti phase twist mode(41626 rad/s).

where,

$$\boldsymbol{m} = \begin{bmatrix} m_{Lx}+m_{Lc} & 0 & 0 & 0 \\ 0 & m_{Ly}+m_{Lc} & 0 & 0 \\ 0 & 0 & m_{Rx}+m_{Rc} & 0 \\ 0 & 0 & 0 & m_{Ry}+m_{Rc} \end{bmatrix},$$

$$\boldsymbol{D} = \begin{bmatrix} x_l \\ y_l \\ x_r \\ y_r \end{bmatrix}, \quad \boldsymbol{Q} = \begin{bmatrix} Q_{Lx} & 0 & 0 & 0 \\ 0 & Q_{Ly} & 0 & 0 \\ 0 & 0 & Q_{Rx} & 0 \\ 0 & 0 & 0 & Q_{Ry} \end{bmatrix},$$

$$\boldsymbol{F} = \begin{bmatrix} F_{Ldrive} \\ -2m_{Lc}\Omega_z\dot{x}_l + F_{Lyfc} \\ F_{Rdrive} \\ -2m_{Rc}\Omega_z\dot{x}_R + F_{Ryfc} \end{bmatrix},$$

$$\boldsymbol{\omega} = \begin{bmatrix} \omega_{Lx} & 0 & 0 & 0 \\ 0 & \omega_{Ly} & 0 & 0 \\ 0 & 0 & \omega_{Rx} & 0 \\ 0 & 0 & 0 & \omega_{Ry} \end{bmatrix}$$

$$= \mathrm{diag}\left[\sqrt{\frac{2k_{Lx}+k_{con}}{2\left(m_{Lx}+m_{Lc}\right)}}, \sqrt{\frac{k_{Ly}}{m_{Ly}+m_{Lc}}},\right.$$

$$\left.\sqrt{\frac{2k_{Rx}+k_{con}}{2\left(m_{Rx}+m_{Rc}\right)}}, \sqrt{\frac{k_{Ry}}{m_{Ry}+m_{Rc}}}\right]$$

are the mass, displacement, quality factor, external force and resonant frequency matrix respectively; $m_{Lx} = m_{Rx}$, $m_{Ly} = m_{Ry}$ and $m_{Lc} = m_{Rc}$ are the equivalent mass of left drive frame, right drive frame, left sense frame, right sense frame, left Coriolis mass and right Coriolis mass; $k_{Lx} = k_{Rx}$, $k_{Ly} = k_{Ry}$ and k_{con} are the equivalent stiffness of left drive mode, right drive mode, left sense mode, right sense mode and connect spring; x_l, x_r and $Q_{Lx} = Q_{Rx}$ are left and right drive (anti-phase) mode displacement and quality factor; y_l, y_r and $Q_{Ly} = Q_{Ry}$ are left and right sense mode displacements and quality factors; Ω_z is angular rate input; sense frame masses $m_{Ly} = m_{Ry} \ll m_{Lc} = m_{Rc}$; drive mode electrostatic force $F_{Ldrive} = F_{Rdrive} = F_d sin(\omega_d t)$, F_d and ω_d are drive mode stimulating magnitude and frequency; $F_{Lyfc} = F_{Ryfc}$ are left and right sense mode feedback forces. For an ideal structure (ignore the manufacture error), the left and right system should have the symmetrical moving characteristic, so we have $x = x_l = -x_r$, $Q_{Lx} = Q_{Rx} = Q_x$, $Q_{Ly} = Q_{Ry} = Q_y$, $\omega_{Lx} = \omega_{Rx} = \omega_x$, $\omega_{Ly} = \omega_{Ry} = \omega_y$, and the sense mode movement is the superposition of 2nd and 3rd modes, then the displacement of drive and sense modes can be got from equation (1) as:

$$x(t) = \frac{F_d/m_x}{\sqrt{\left(\omega_x^2-\omega_d^2\right)^2+\omega_x^2\omega_d^2/Q_x^2}}\sin(\omega_d t+\varphi_x)$$

$$+ \frac{F_d\omega_x\omega_d/m_xQ_x}{\left(\omega_x^2-\omega_d^2\right)^2+\omega_x^2\omega_d^2/Q_x^2}e^{-\frac{\omega_x}{2Q_x}t}$$

$$\times \cos(\sqrt{1-1/4Q_x^2}\omega_x t)$$

$$+ \frac{F_d\omega_d\left(\omega_x^2/Q_x^2+\omega_d^2-\omega_x^2\right)/m_x}{\omega_x\sqrt{1-1/4Q_x^2}\left[\left(\omega_x^2-\omega_d^2\right)^2+\omega_x^2\omega_d^2/Q_x^2\right]}$$

$$\times e^{-\frac{\omega_x}{2Q_x}t}\sin(\sqrt{1-1/4Q_x^2}\omega_x t) \tag{2}$$

$$y(t) = \frac{\frac{-2\Omega_z\omega_dF_d}{m_x\sqrt{\left(\omega_x^2-\omega_d^2\right)^2+\omega_x^2\omega_d^2/Q_x^2}}}{\sqrt{\left(\omega_y^2-\omega_d^2\right)^2+\omega_y^2\omega_d^2/Q_y^2}}\sin(\omega_d t+\varphi_x+\frac{\pi}{2}+\varphi_y)$$

$$+ \frac{\frac{2\Omega_z\omega_dF_d}{m_x\sqrt{\left(\omega_x^2-\omega_d^2\right)^2+\omega_x^2\omega_d^2/Q_x^2}}}{\left(\omega_y^2-\omega_d^2\right)^2+\omega_y^2\omega_d^2/Q_y^2}$$

$$\left[\omega_y\omega_d\sin\varphi_x/Q_y+\left(\omega_y^2-\omega_d^2\right)\cos\varphi_x\right]$$

$$\times e^{-\frac{\omega_y}{2Q_y}t}\cos(\sqrt{1-1/4Q_y^2}\omega_y t)$$

$$+ \frac{-2\Omega_z\omega_dF_d}{m_x\sqrt{\left(\omega_x^2-\omega_d^2\right)^2+\omega_x^2\omega_d^2/Q_x^2}}$$
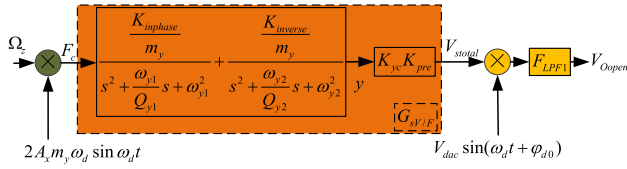
FIGURE 4. The dual-mass MEMS gyroscope sensing open-loop system schematic.

$$\times\, e^{-\frac{\omega_y}{2Q_y}t}\sin\left(\sqrt{1-1\big/4Q_y^2}\,\omega_y t\right)$$

$$\times\, \frac{\left[\omega_y\left(\omega_y^2-3\omega_d^2\right)\cos\varphi_x\big/(2Q_y)\right.}{\left.+\omega_d\left(\omega_y^2\big/\left(2Q_y^2\right)+\omega_y^2-\omega_d^2\right)\sin\varphi_x\right]}{\omega_y\sqrt{1-1\big/4Q_x^2}\left[\left(\omega_y^2-\omega_d^2\right)^2+\omega_y^2\omega_d^2\big/Q_y^2\right]}$$

(3)

where, $\varphi_x=-tg^{-1}\left(\frac{\omega_x\omega_d}{Q_x\left(\omega_x^2-\omega_d^2\right)}\right)$, $\varphi_y=-tg^{-1}\left(\frac{\omega_y\omega_d}{Q_y\left(\omega_y^2-\omega_d^2\right)}\right)$ and in the drive closed-loop, we have $\omega_x=\omega_d$, and we get:

$$\begin{cases} x(t)=\dfrac{F_d Q_x}{m_x\omega_d^2}\cos(\omega_d t)=A_x\cos(\omega_d t) \\[2mm] y(t)=\dfrac{-2\Omega_z F_d Q_x}{m_x\omega_d\sqrt{\left(\omega_y^2-\omega_d^2\right)^2+\omega_y^2\omega_d^2\big/Q_y^2}}\sin(\omega_d t) \\[2mm] \qquad = A_y\sin(\omega_d t). \end{cases}$$

(4)

III. SENSING CLOSED-LOOP DESIGN

A. SENSING OPEN-LOOP ANALYSYS

The dual-mass MEMS gyroscope sensing closed-loop is based on open-loop system, whose schematic is shown in Figure. 4.

In the above figure, K_{yc} and K_{pre} are displacement to capacitance transform function and pre-amplifier; K_{amp} is second differential amplifier; F_{LPF1} is second order low pass filter, F_{BTCPC} is the controller; K_{FBy} is voltage-force interface transform coefficient of force rebalances combs; $K_{inphase}$ and $K_{inverse}$ are displace-voltage transform parameters of sensing in-phase and anti-phase modes, and the equations can be got:

$$F_c(t)=2\Omega_z(t)\,m_y A_x\omega_d\sin\omega_d t \tag{5}$$

$$V_{stotal}(s)=F_c(s)\,G_{sV/F} \tag{6}$$

$$V_{Oopen}=V_{dac}\sin(\omega_d t+\varphi_{d0})V_s F_{LPF1} \tag{7}$$

$$G_{sV/F}=\left(\frac{K_{inphase}}{s^2+\frac{\omega_{y1}}{Q_{y1}}s+\omega_{y1}^2}+\frac{K_{inverse}}{s^2+\frac{\omega_{y2}}{Q_{y2}}s+\omega_{y2}^2}\right)K_{yc}K_{pre} \tag{8}$$

And it can be got after the Laplace transform:

$$V_{stotal}(s)=A_x\omega_d K_{yc}K_{pre}(\Omega_z(s-j\omega_d)+\Omega_z(s+j\omega_d))$$
$$\times\left(\frac{K_{inphase}}{s^2+\frac{\omega_{y1}}{Q_{y1}}s+\omega_{y1}^2}+\frac{K_{inverse}}{s^2+\frac{\omega_{y2}}{Q_{y2}}s+\omega_{y2}^2}\right) \tag{9}$$

Substitute Equation (9) into (7) and we have:

$$V_{Oopen}(s)$$
$$=\frac{1}{2}A_x\omega_d V_{dac}K_{yc}K_{pre}F_{LPF1}(s)$$
$$\times\left\{\begin{array}{l}\left(\dfrac{[\Omega_z(s)+\Omega_z(s+2j\omega_d)]\,e^{-j\varphi_{d0}}K_{inphase}}{(s+j\omega_d)^2+\frac{\omega_{y1}}{Q_{y1}}(s+j\omega_d)+\omega_{y1}^2}\right.\\ \qquad\left.+\dfrac{[\Omega_z(s)+\Omega_z(s+2j\omega_d)]\,e^{-j\varphi_{d0}}K_{inverse}}{(s+j\omega_d)^2+\frac{\omega_{y2}}{Q_{y2}}(s+j\omega_d)+\omega_{y2}^2}\right)\\ +\left(\dfrac{[\Omega_z(s-2j\omega_d)+\Omega_z(s)]\,e^{j\varphi_{d0}}K_{inphase}}{(s-j\omega_d)^2+\frac{\omega_{y1}}{Q_{y1}}(s-j\omega_d)+\omega_{y1}^2}\right.\\ \qquad\left.+\dfrac{[\Omega_z(s-2j\omega_d)+\Omega_z(s)]\,e^{j\varphi_{d0}}K_{inverse}}{(s-j\omega_d)^2+\frac{\omega_{y2}}{Q_{y2}}(s-j\omega_d)+\omega_{y2}^2}\right)\end{array}\right\}$$

(10)

The low pass filter F_{LPF1} cut off the high frequency signal and ignore the demodulator phase error (make $\varphi_{d0}=0$), and Equation (10) can be expressed as:

$$\left|\frac{V_{Oopen}(s)}{\Omega_z(s)}\right|=\left|\frac{1}{2}A_x\omega_d V_{dac}K_{yc}K_{pre}F_{LPF1}(s)G_{equal}(s)\right| \tag{11}$$

where,

$$G_{equal}(s)$$
$$=\left[\frac{K_{inphase}(s^2+\frac{\omega_{y1}}{Q_{y1}}s+\omega_{y1}^2-\omega_d^2)}{(s^2+\frac{\omega_{y1}}{Q_{y1}}s+\omega_{y1}^2-\omega_d^2)^2+(2s\omega_d+\frac{\omega_{y1}}{Q_{y1}}\omega_d)^2}\right.$$
$$\left.+\frac{K_{inverse}(s^2+\frac{\omega_{y2}}{Q_{y2}}s+\omega_{y2}^2-\omega_d^2)}{(s^2+\frac{\omega_{y2}}{Q_{y2}}s+\omega_{y2}^2-\omega_d^2)^2+(2s\omega_d+\frac{\omega_{y2}}{Q_{y2}}\omega_d)^2}\right]$$

In Equation (11), the transform function of the MEMS gyroscope sensing open-loop is shown, and its Bode Map is shown in Fig.5. And the static scale factor can be got when s=0 (12), as shown at the bottom of the next page.

Because, $(\omega_{y1,2}^2-\omega_d^2)\gg\frac{\omega_{y1,2}}{Q_{y1,2}}\omega_d$ and $K_{inverse}\gg K_{inphase}$, then, the gyroscope open-loop scale factor can be expressed as:

$$\left|\frac{V_{Oopen}(s)}{\Omega_z(s)}\right|$$
$$=\frac{A_x V_{dac}K_{yc}K_{pre}K_{inverse}F_{LPF1}(s)(s^2+\frac{\omega_{y2}}{Q_{y2}}s+\omega_{y2}^2-\omega_d^2)}{(s^2+\frac{\omega_{y2}}{Q_{y2}}s+\omega_{y2}^2-\omega_d^2)^2+(2s\omega_d+\frac{\omega_{y2}}{Q_{y2}}\omega_d)^2} \tag{13}$$

B. SENSING CLOSED-LOOP DESIGN AND ANALYSYS

The MEMS gyroscope sensing closed-loop system is shown in Figure. 6. The system is based on sensing open-loop, and the following equations can be got from Fig. 6.

$$V_s(s)=K_{yc}K_{pre}K_{amp}\left(F_c(s)-F_{yfc}(s)\right)$$
$$\times\left(\frac{K_{inphase}}{s^2+\frac{\omega_{y1}}{Q_{y1}}s+\omega_{y1}^2}+\frac{K_{inverse}}{s^2+\frac{\omega_{y2}}{Q_{y2}}s+\omega_{y2}^2}\right) \tag{14}$$
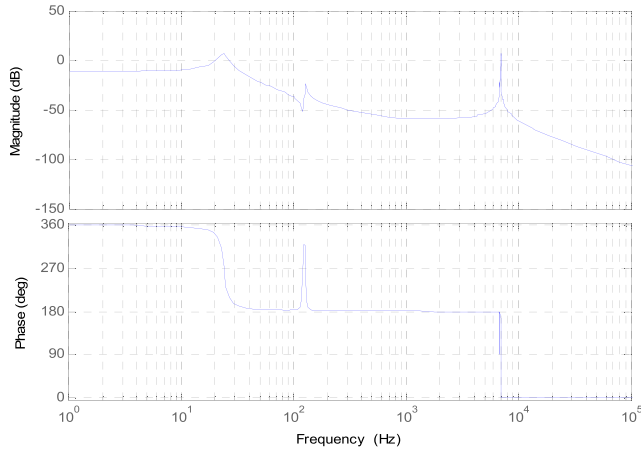
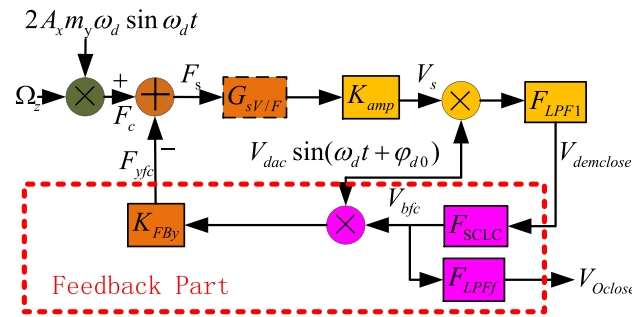**FIGURE 5.** The MEMS gyroscope sensing open-loop system Bode Map.

FIGURE 6. The schematic of MEMS gyroscope sensing closed-loop.

$$V_{bfc}(t) = V_{demclose}(t) F_{SCLC} \tag{15}$$

$$F_{yfc}(t) = K_{FBy} V_{bfc}(t) V_{dac} \sin(\omega_d t + \varphi_{d0}) \tag{16}$$

$$V_{Oclose} = V_{bfc} F_{LPFf} \tag{17}$$

Also, employ the same method used in Equation (10) and (11), and we get:

$$
\begin{aligned}
V_{demclose}(s) &= \frac{V_{dac}}{2} K_{yc} K_{pre} K_{amp} F_{LPF1}(s) \\
&\times \left(A_x \omega_d \Omega_z(s) - \frac{V_{dac} K_{FBy} V_{bfc}(s)}{2m_y} \right) G_{equal}(s) \tag{18}
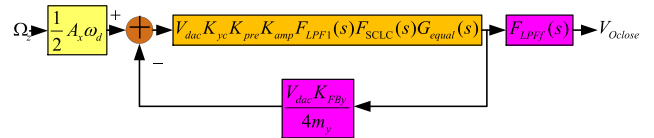\end{aligned}
$$

FIGURE 7. MEMS gyroscope sensing closed-loop system diagram.

The following equation can be got from Equation (18), (15), and (19), as shown at the bottom of this page.

Then the sensing closed-loop system controlling diagram can be express in Fig.7:

From the Equation (19) and Fig. 7 it is obviously that the key point of the system is the controller F_{SCLC}, in this work, we employ a big value of F_{SCLC}, and make:

$$\frac{V_{dac}^2 K_{FBy}}{4m_y} K_{yc} K_{pre} K_{amp} F_{LPF1}(s) F_{SCLC}(s) G_{equal}(s) \gg 1$$

Then, Equation (19) can be simplified as:

$$\left| \frac{V_{Oclose}(s)}{\Omega_z(s)} \right| = \left| \frac{2m_y F_{LPFf}(s) A_x \omega_d}{K_{FBy} V_{dac}} \right| \tag{20}$$

From the Equation (20) it can be seen that the scale factor of sensing closed-loop does not have relationship with the sense mode resonant frequency. And different F_{SCLC} values are investigated to verify the stability of the system. The value of F_{SCLC} was choose as: 0.1, 1, 10, 50, 100, 200, 300, 400, 500, 1000, 2000, 5000, 10000, and the Pole-Zero Map was shown in Fig. 8. And when $F_{SCLC} > 500$, the poles appeared in positive half real axis, which makes the system unstable. So the F_{SCLC} should be designed carefully and should satisfy the following requirement [16]:

(1). F_{SCLC} should have large enough gain in low frequency part, which provides low controlling error and enhance the static capability of the gyroscope.

(2). In middle frequency stage F_{SCLC} should expand the bandwidth of the gyroscope, which improve the dynamic performance of the gyroscope.

(3). Outside the bandwidth frequency stage, F_{SCLC} should decrease the high frequency noise signal, and improve the signal-noise rate of the gyroscope.

$$
\left| \frac{V_{Oopen}(0)}{\Omega_z(0)} \right| = \left| \frac{1}{2} A_x \omega_d V_{dac} K_{yc} K_{pre} F_{LPF1}(0) \times \left\{ \frac{K_{inphase}(\omega_{y1}^2 - \omega_d^2)}{(\omega_{y1}^2 - \omega_d^2)^2 + (\frac{\omega_{y1}}{Q_{y1}} \omega_d)^2} + \frac{K_{inverse}(\omega_{y2}^2 - \omega_d^2)}{(\omega_{y2}^2 - \omega_d^2)^2 + (\frac{\omega_{y2}}{Q_{y2}} \omega_d)^2} \right\} \right| \tag{12}
$$

$$
\left| \frac{V_{Oclose}(s)}{\Omega_z(s)} \right| = \left| \frac{2 V_{dac} K_{yc} K_{pre} K_{amp} F_{LPF1}(s) F_{SCLC}(s) F_{LPFf}(s) A_x \omega_d G_{equal}(s)}{4 + \frac{V_{dac}^2 K_{FBy}}{m_y} K_{yc} K_{pre} K_{amp} F_{LPF1}(s) F_{SCLC}(s) G_{equal}(s)} \right| \tag{19}
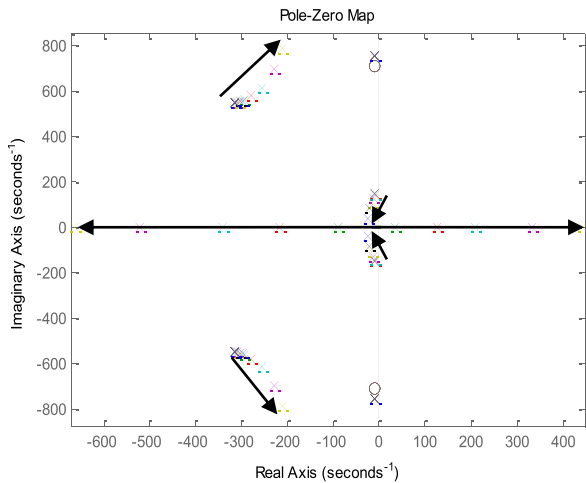$$

FIGURE 8. Pole-Zero Map of sensing closed-loop with different F_{SCLC} values.

Then, the transfer function of F_{SCLC} can be expressed as:

$$F_{SCLC}(s) = \frac{K_{pi}s^2 + 2K_{pi}\omega_{pi1}s + K_{pi}\omega_{pi1}^2}{s^2 + \omega_{pi2}s} \quad (21)$$

C. MEMS GYROSCOPE SENSING CLOSED-LOOP SYSTEM SIMULATION

In MATLAB Simulink environment, we build up the model of MEMS gyroscope sensing closed-loop, which is as shown in Fig. 9. Basically, four closed-loops are configured in the model: drive closed-loop, two quadrature error correction closed-loops for left and right mass structure [22] and sensing closed-loop. And based on this system, the schematic is shown in Fig.10 [8]:

In drive closed-loop, the signal is processed as following steps:

(1). Drive mode displacement signal conversion and amplification: the displacement $x(t)$ of drive frame is detected by drive sense combs and processed by differential instrument amplifier in part ①.

(2). Stimulation signal alternating part modulation reference signal preparation: the differential module ② generates a 90° phase difference to meet the phase condition of drive signal modulator reference $V_{dac}Sin(\omega_d t)$.

(3). Signal amplitude pick up, compare and controlling: the amplitude of $V_{dac}Sin(\omega_d t)$ is detected and valued by full-wave rectifier in module ③ and a low pass filter in part ④. And, in module ⑤, V_{dac} is added with voltage V_{ref} ⑥, then, drive PI controller ⑦ generates the control signal based on the adding consequence.

(4). Stimulation signal form stage: the control signal is modulated by $V_{dac}Sin(\omega_d t)$ in module ⑧ to generate the drive signal alternating part and after that, in part ⑩, the signal is added with direct current voltage V_{DC} in module ⑨ to generate electrostatic force to stimulate the drive mode.

The sensing closed-loop system is processed as following:

(1). Sense mode displacement signal conversion and amplification: the Coriolis masses' movement is picked up by sense frame, and are detected separately by same instrument differential interface as drive loop pre amplifiers ⑪. Then the signal is enlarged through second differential amplifier ⑫ and generate the sense frame (mode) movement total signal V_s.

(2). Sense mode displacement signal demodulation: V_s is demodulated by reference signal $V_{dac}Sin(\omega_d t)$ (in module ⑬) and generates the demodulated signal V_{sdem}. Then, low pass filter F_{LPF1} in module ⑭ cut off the high frequency part of the signal V_{sdem}.

(3). Sensing closed-loop output: The output signal of F_{LPF1} is the controlling reference signal of F_{SCLC} in module ⑮, and F_{SCLC} generates the feedback signal, which forms the final closed-loop output signal V_{Oclose} after the low pass filter F_{LPFf} in part ⑯.

(4). Sense feedback channel: the output of F_{SCLC} is modulated by reference $V_{dac}Sin(\omega_d t)$ and formed feedback alternating part. And the feedback direct current part is V_{FDC} in module ⑳ two parts are added in parts ⑱ and ⑲. Then, the sense loop feedback signal is finished and apply to the force rebalances combs.

The quadrature error correction closed-loop system employs left and right mass independent correction method and the correction technology is based on coupling stiffness correction method. So, it includes two same closed-loops and the signal is processed as following [22]:

(1). Quadrature error demodulation: the left and right mass sense frame displacement signals are picked up separately in module ⑪, and the output signals of module ⑪ are sent to demodulator ㉑ and demodulated by drive mode displacement in-phase signal from drive closed-loop.

(2). Quadrature error compensation: the demodulated signals are processed by low pass filters and are compared by reference signal VQREF (module ㉒) through parts ㉓.

(3). Quadrature error correction controlling signal: the results of compensation are sent to quadrature error controller in module ㉔, and generate two independent controlling signals to quadrature error correction combs to correct the quadrature error signal.

Four closed-loops are independent and aim different object signals.

The simulation results of the model in Fig. 9 is shown in Fig. 11, including sensing open-loop and closed-loop.

In Fig. 11, sensing open-loop output signal V_{Oopen} is steady after 1s when the system is "power on", and an angular rate with $\Omega_z=100$ °/s is input when time is 3s, and at 3.5s the system back to steady state. During this stage, the peak value of sense mode displacement y is about 0.08um.

When the sense loop is closed, as shown in Fig. 11, the output signal V_{Oclose} is stable less than 0.5s after "power on", and also, input with $\Omega_z=100$ °/s at 3s, the system returns to steady state at 3.3s, and the sense mode displacement is 0.1nm, which is far smaller (about 800 times) than the
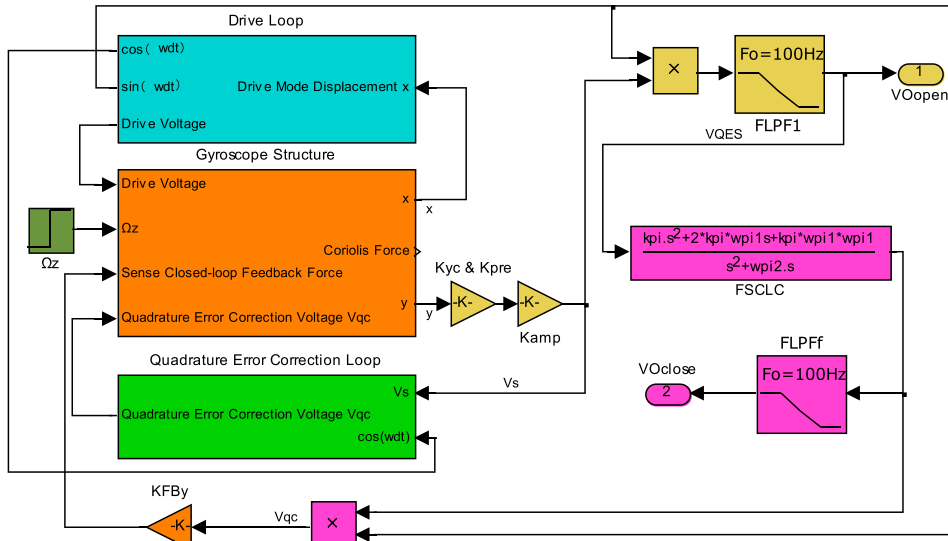
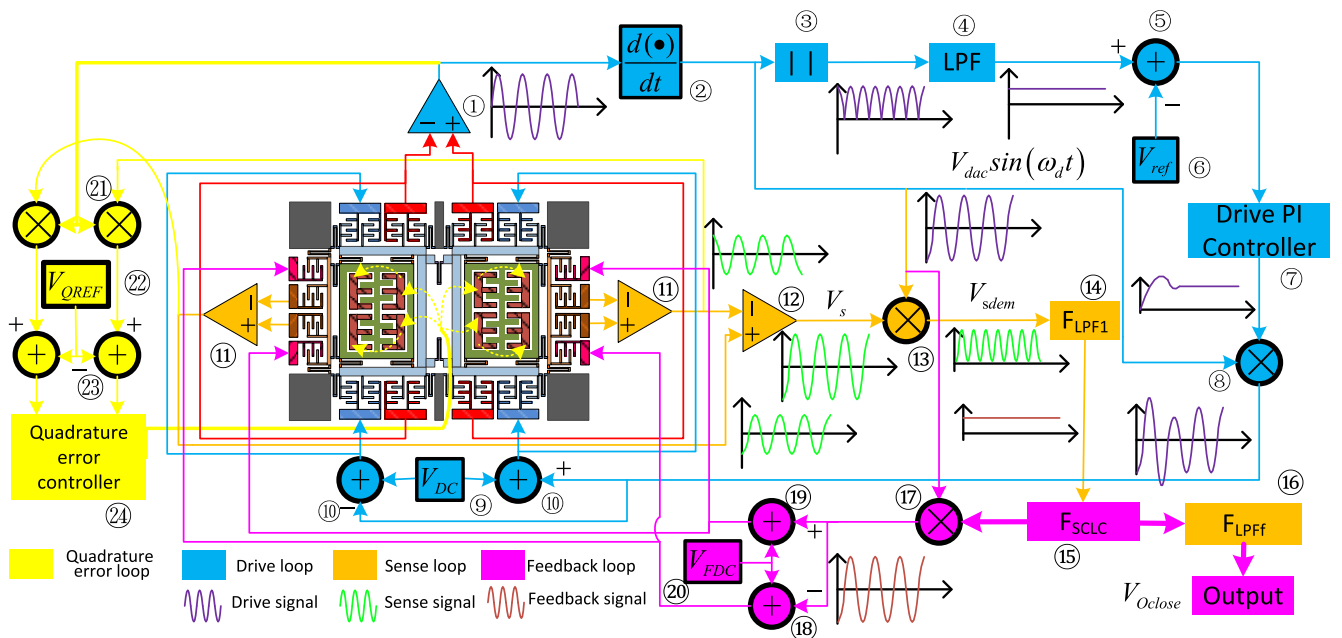**FIGURE 9.** The Simulink modal of MEMS gyroscope sensing closed-loop.

FIGURE 10. Four closed-loop MEMS gyroscope monitoring system schematic.

open loop state. And the simulation proves the stability and speedability of the sensing closed-loop.

IV. EXPERIMENT

A. EXPERIMENT PLATFORM AND EQUIPMENT

The MEMS gyroscope prototype tested in this paper is developed by our team. The prototype includes the following part:

(1). The gyroscope structure: is processed by MEMS technology, Deep Reactive Ion Etching (DRIE) and

Silicon on Glass (SOG) processing methods are utilized.

(2). The chip level package: vacuum ceramics shell is employed to provide the high Q value for the structure.

(3). Analog circuits: 3 PCB boards are employed and:

PCB I: including drive closed-loop and pre-amplifiers of sense loop. And according with module ①-⑪ in Fig.10.

PCB II: containing two independent quadrature error correction closed-loops for left and right
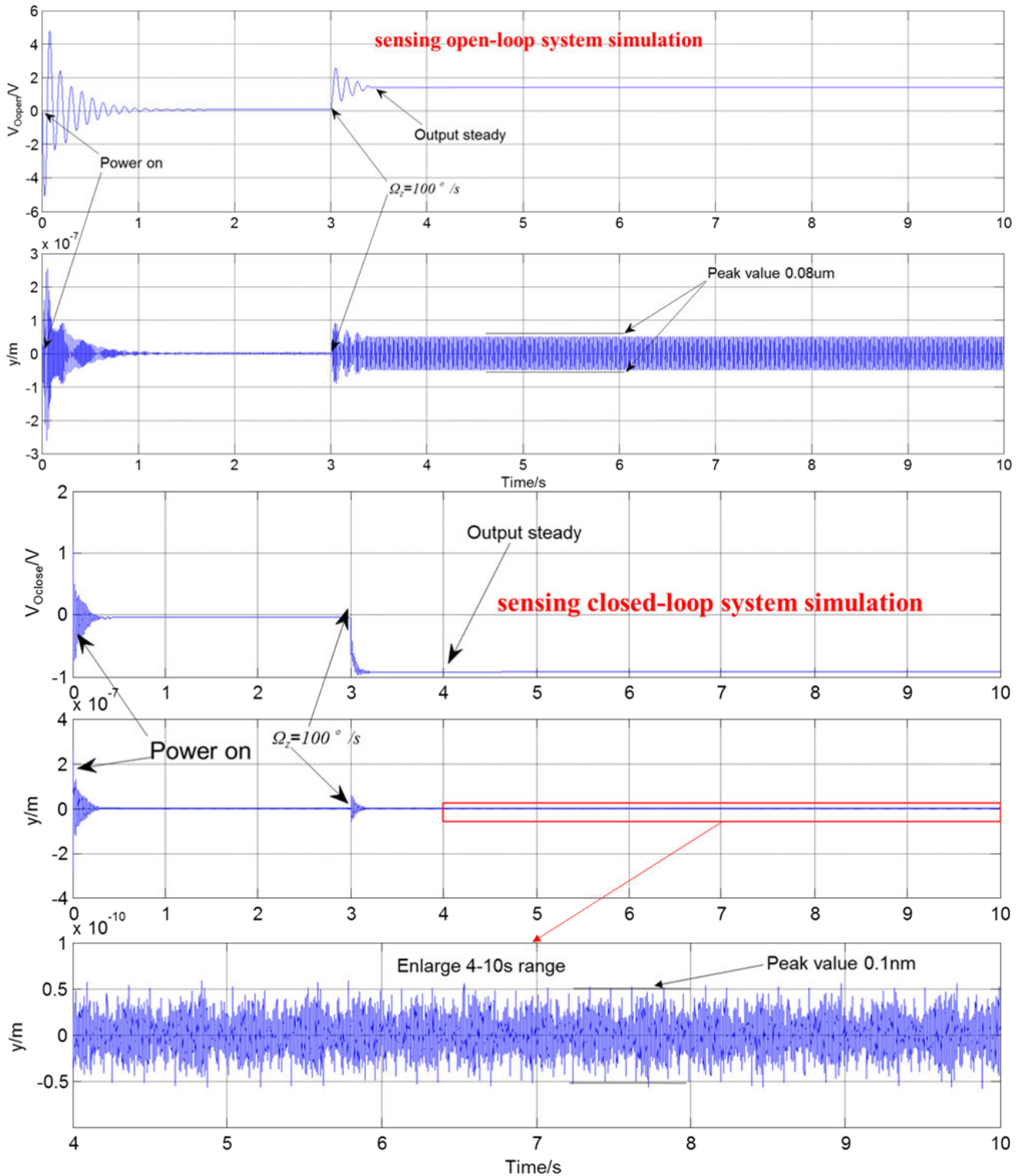
FIGURE 11. MEMS gyroscope simulation results.

masses. And according with module ㉑-㉔ in Fig.10.

PCB III: arranged the sense open and closed-loop. And according with module ⑫-⑳ in Fig.10.

(4). Overall: the prototype size is $46*46*36mm^3$, the power supply is $\pm 8V$ DC voltage and GND, the power consumption is about 560mW, outside package is steel shell.
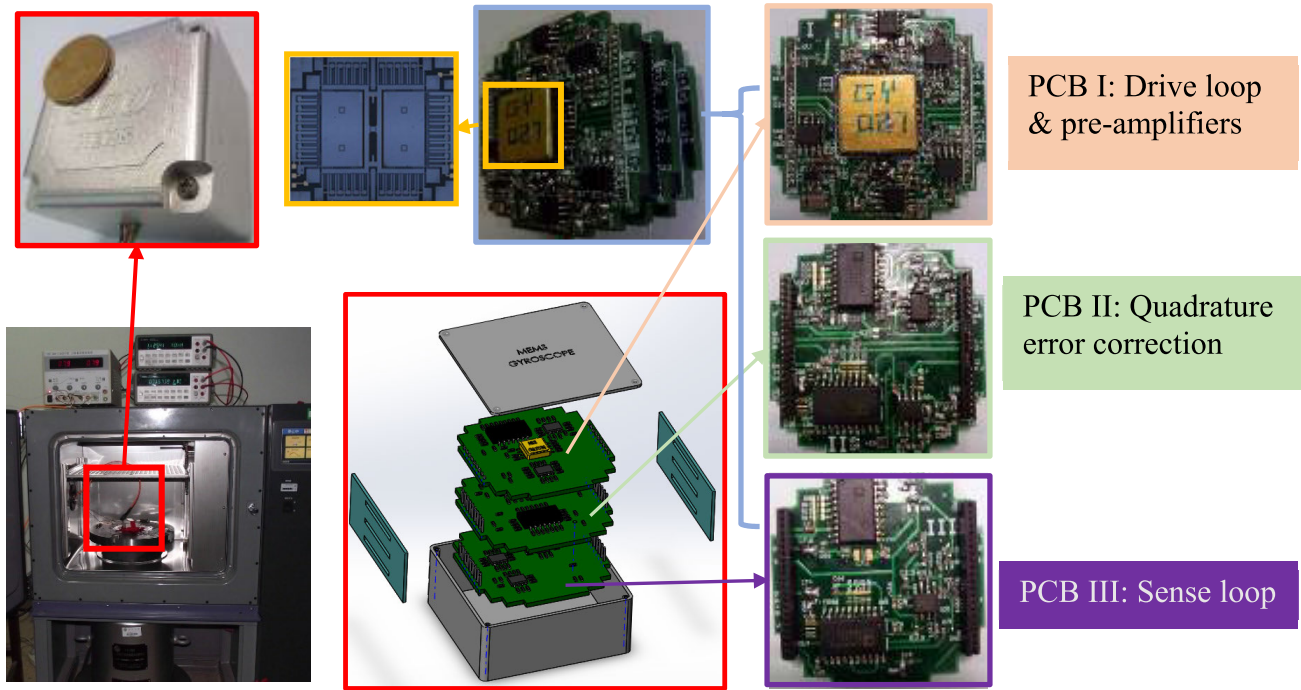
FIGURE 12. MEMS gyroscope prototype and test platform.

The test equipment including: oscilloscope (Agilent DSO7104B), multimeter (Agilent 34401A), digital power (Agilent E3631A), the signal generator (Agilent 33220A), temperature oven, and turntable. The prototype and equipment are shown in Fig. 12.

B. STATIC TEST

The static tests steps are:

(1). Preparation: stable the turntable, open the oven door and let the inside temperature of gyroscope equal to the environment temperature, and 1Hz sampling rate is set.

(2). Data collection: detect the sensing open-loop output signal V_{Oopen} for 4800 points, pick up sensing closed-loop output signal V_{Oclose} six groups and 4800 points each group. Power off at least 1 hour after each 4800 points to make sure the gyroscope is cool.

(3). Scale factor calculation: make $\Omega_z = \pm 100°/s$, and read the gyroscope output to calculate the scale factor.

The static test curves of drive mode movement signal (selected up from module ①) and sense mode movement signals (picked up from module ⑫) under sensing open-loop and closed-loop conditions are captured by oscilloscope and shown in Fig. 13. It is obviously that in open loop, the phase of sense output signal is 90 degree difference with drive mode, and the amplitude is about 750mV (peak-peak value). And in closed-loop, the sense mode movement is only noise left, no frequency and phase characteristic can be observed, which verified the simulation results in Fig. 11.

The Allan derivation of the static tests are shown in Fig. 15, and the bias stability of sensing open-loop and sensing closed-loop five tests are 2.168 °/h and 0.445 °/h, 0.460 °/h, 0.321 °/h, 0.356 °/h, 0.441 °/h and 0.469 °/h respectively.

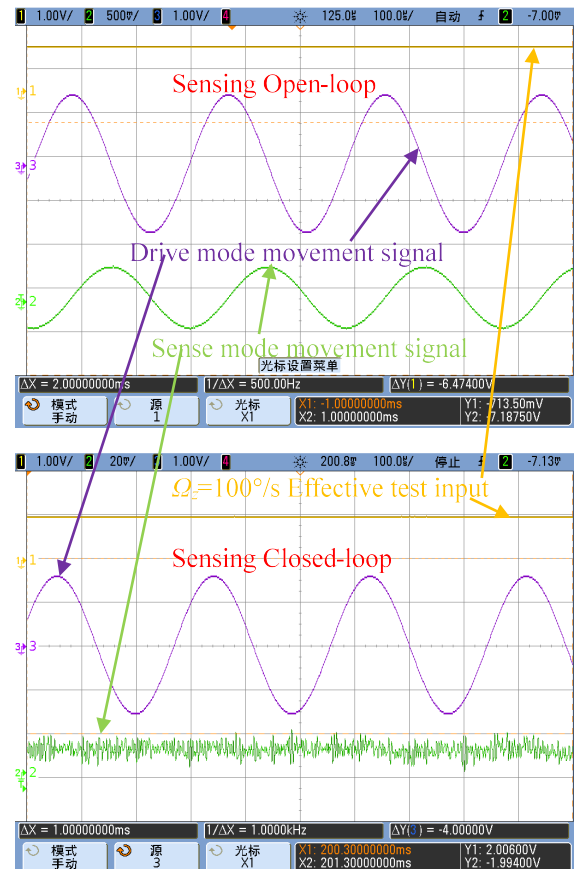**FIGURE 13.** Static tests curves.

The angular random walking values of sensing open-loop and sensing closed-loop five tests are 0.155 °/√h and 0.0416 °/√h, 0.0415 °/√h, 0.0415 °/√h, 0.0413 °/√h,
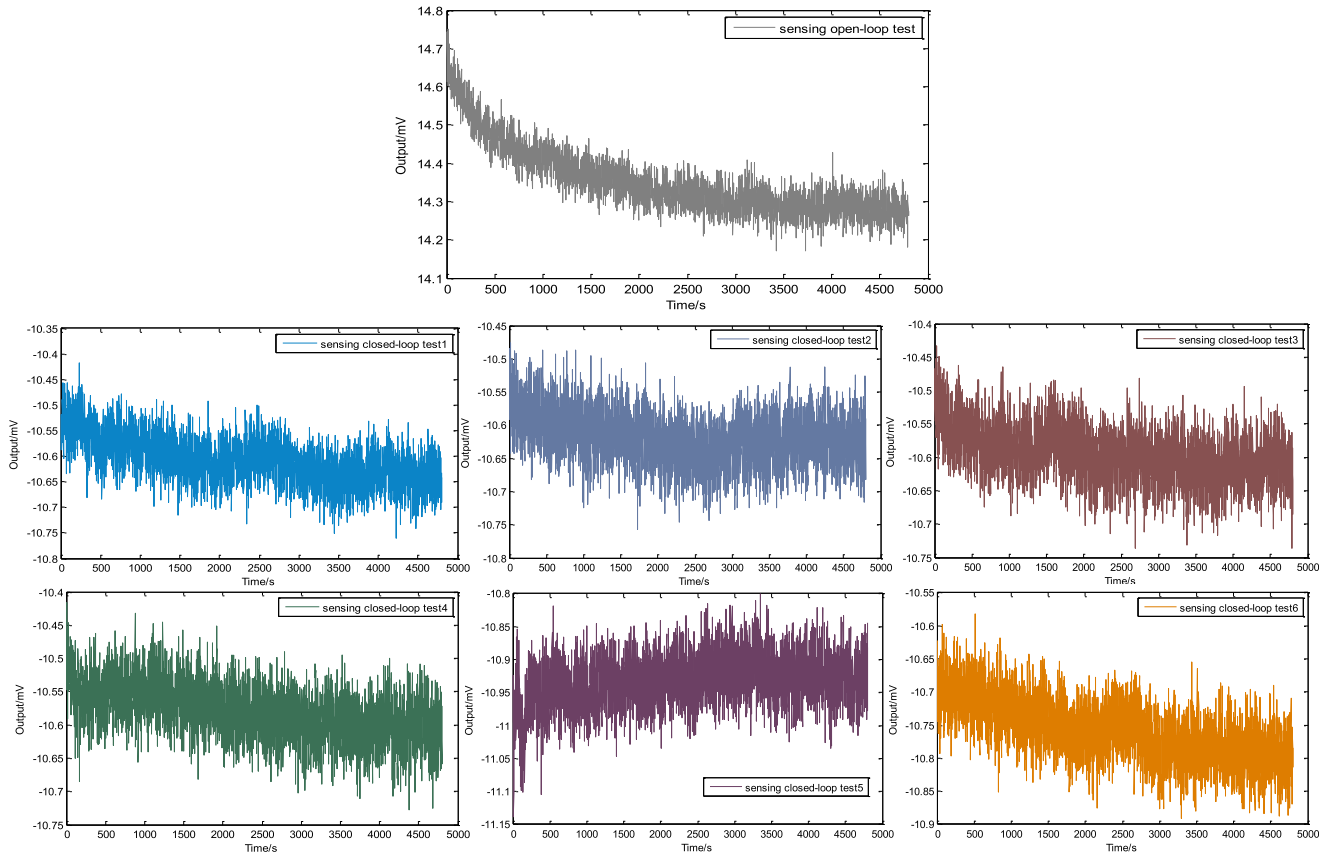
FIGURE 14. Static test output of the gyroscope.

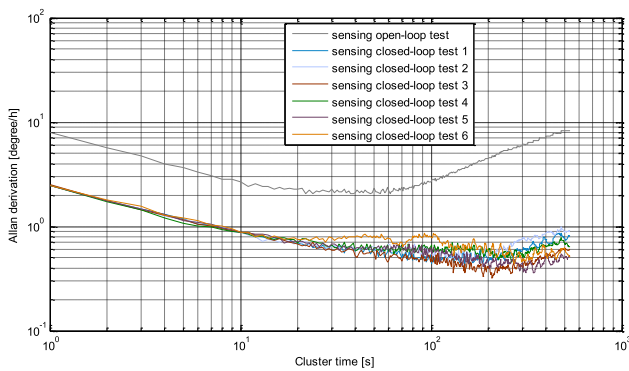**FIGURE 15.** Allan derivation curves of static test.

0.0413 °/√h and 0.0409 °/√h respectively. The results show that the bias stability and angular random walking parameters are improved obviously after the sensing closed-loop is employed.

FIGURE 16. Sensing closed-loop response test.

C. DYNAMIC TEST

In order to test the dynamic characteristic of the sensing closed-loop system, the step response test is arranged. The process of the dynamic experiment is:

(1). Preparing stage: two channels of oscilloscope are connected to signal generator and sense mode movement y. And the trigger is set with signal generator and up edge is valid.

(2). Angular rate effective voltage: the force rebalancing combs stimulation method is employed [16], and the $\Omega_z = 100°/s$ effective angular rate is calculated as about 1V and the signal generator provide the voltage.

With the above two step, the dynamic test is done and the signal curves are shown in Fig. 16. The peak value of the sense mode movement is about 50mV and after about 120ms

TABLE 1. Gyroscope scale factor experiment.

| State	Test	Clockwise Scale Factor (mV/°/s)	Anticlockwise Scale Factor (mV/°/s)	Scale factor (mV/°/s)	Nonlinearity (ppm)	Asymmetry (ppm)	Repeatability (ppm)
Sensing Open-loop	Test 1	-10.0234	-10.0268	-10.0260	511	398	
	Test 2	-10.0296	-10.0251	-10.0294	659	499	403
	Test 3	-10.0339	-10.0034	-10.0206	811	392	
	Average	-	-	-10.0253	660	430	
Sensing Closed-loop	Test 1	9.29612	9.29674	9.29662	69.87	66.7	
	Test 2	9.29673	9.29745	9.29718	39.04	76.4	50.4
	Test 3	9.29616	9.29657	9.29625	68.9	44.1	
	Average	-	-	9.29668	59.27	62.4	
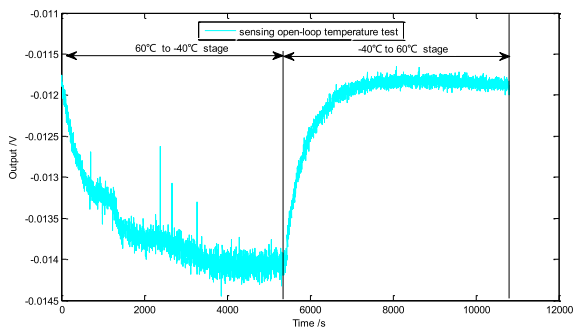
FIGURE 17. MEMS gyroscope sensing open-loop temperature test.

FIGURE 18. MEMS gyroscope sensing open-loop temperature test.
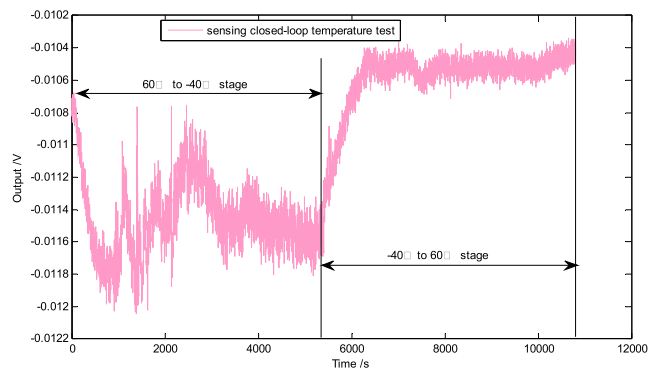

FIGURE 19. Sensing open-loop scale factor test.
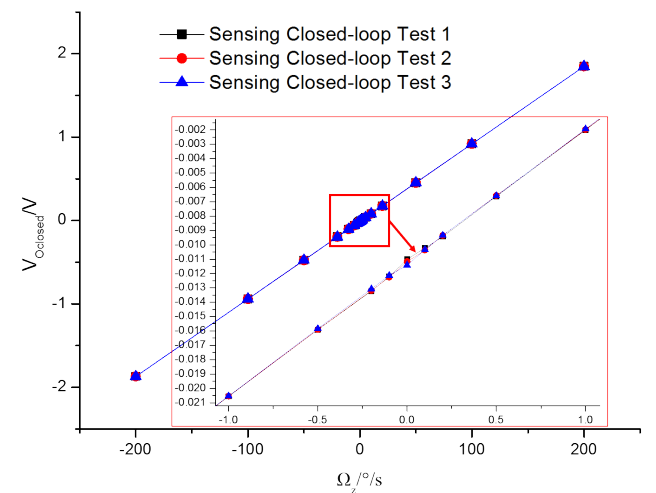
FIGURE 20. Sensing closed-loop scale factor test.

the sense mode returns to stable state (as same as before step signal input), which verify the speedability and stability.

D. TEMPERATURE TEST

The temperature range of the experiment is −40° to 60°, sampling rate is 1Hz. The temperature is set up to 60°, and down to −40°, stay one hour and up to 60°, and keep one hour. The full temperature range output signal of sensing open-loop and closed-loop are shown in Fig. 17 and Fig.18.

The max and min values of sensing open-loop and closed-loop are −11.3115mV, −14.2607mV, −10.4002mV and −11.3272mV, respectively.

Sensing open-loop and closed-loop bandwidth values are 13 and 104Hz, which were tested through turntable.

E. SCALE FACTOR TEST

The scale factor experiments are finished on the turntable, and three tests are arranged to verify the repeatability of scale factor. The open-loop and closed-loop scale factor tests results are shown in Fig.19 and Fig. 20. The MEMS gyroscope scale factor experiment results under room temperature

TABLE 2. Gyroscope scale factor temperature experiment.

State	Test	+1°/s (mV)	-1°/s (mV)	Scale factor (mV/°/s)	Scale factor Temperature coefficient (ppm/℃)
Sensing Open-loop	60℃	-22.018	-1.6055	-10.2061	
	-40℃	-23.920	-4.1623	-9.87869	180
	20℃	-	-	-10.0253	
Sensing Closed-loop	60℃	-1.6302	-20.191	9.28037	
	-40℃	-2.4397	-20.980	9.26999	28.7
	20℃	-	-	9.29668	

TABLE 3. Gyroscope test conclusion.

Parameter	Open-loop	Closed-loop
Bias stability (°/h)	2.168	0.445 0.460 0.321 0.356 0.441 0.469
Angular random walk (°/√h)	0.155	0.0416 0.0415 0.0415 0.0413 0.0413 0.0409
Bias temperature coefficient (°/h/℃)	10.59	3.59
Bandwidth (Hz)	13	104
Scale Factor (mV/°/s)	-10.0253	9.29668
Scale Factor Nonlinearity (ppm)	660	59.3
Scale Factor Asymmetry (ppm)	430	62.4
Scale Factor Repeatability (ppm)	403	50.4
Scale Factor Temperature Coefficient (ppm/℃)	180	28.7

are shown in Table 1, and the temperature experiment results are shown in Table 2.

V. CONCLUSION AND DISCUSSION

This paper proposed a sensing closed-loop controller system for dual-mass gyroscope, and the controller has advantage on low controlling error, bandwidth expanding and low noise. The sensing closed-loop circuit and system are designed and simulated, and the simulation results show that the sensing closed-loop system is speedability and stability, the sense mode movement is decreased by 800 times after the sensing closed-loop. The four closed-loops system is established on three PCBs by analog circuits, then the experiments results prove the sensing closed-loop advantage. The bias stability

improved 80.9% and reached 0.415 °/h on six time average value. The angular random walk values enhanced 73.3% and the bias temperature coefficients improved 66.1%, the bandwidth value is improved from 13Hz to 104Hz. Meanwhile, scale factor nonlinearity, asymmetry, repeatability and temperature coefficient parameters are optimized by 91.0%, 85.5%, 87.5% and 84.1% respectively. The Coriolis force caused displacement of sense mode was rebalanced and decreased which improved the performance of the gyroscope. The results of the experiment prove the correctness of the design method proposed in this paper.

REFERENCES

[1] K. Tao, L. Tang, J. Wu, S. W. Lye, H. Chang, and J. Miao, "Investigation of multimodal electret-based MEMS energy harvester with impact-induced nonlinearity," *J. Microelectromech. Syst.*, vol. 27, no. 2, pp. 276–288, Apr. 2018.

[2] H. Guo, K. Qian, A. Cai, J. Tang, and J. Liu, "Ordered gold nanoparticle arrays on the tip of silver wrinkled structures for single molecule detection," *Sens. Actuators B, Chem.*, vol. 300, Dec. 2019, Art. no. 126846.

[3] Z. Wang, J. Wang, and W. Du, "Research on fault diagnosis of gearbox with improved variational mode decomposition," *Sensors*, vol. 18, no. 10, p. 3510, Oct. 2018.

[4] D. Xia, C. Yu, and L. Kong, "The development of micromachined gyroscope structure and circuitry technology," *Sensors*, vol. 14, no. 1, pp. 1394–1473, Jan. 2014.

[5] X. Guo, J. Tang, J. Li, C. Shen, and J. Liu, "Attitude measurement based on imaging ray tracking model and orthographic projection with iteration algorithm," *ISA Trans.*, vol. 95, pp. 379–391, Dec. 2019.

[6] Y. Xu, G. Tian, and X. Chen, "Enhancing INS/UWB integrated position estimation using federated EFIR filtering," *IEEE Access*, vol. 6, pp. 64461–64469, 2018.

[7] H. Cao and H. Li, "Investigation of a vacuum packaged MEMS gyroscope architecture's temperature robustness," *Int. J. Appl. Electromagn. Mech.*, vol. 41, no. 4, pp. 495–506, Feb. 2013.

[8] H. Cao, Y. Liu, Y. Zhang, X. Shao, J. Gao, K. Huang, Y. Shi, J. Tang, C. Shen, and J. Liu, "Design and experiment of dual-mass MEMS gyroscope sense closed system based on bipole compensation method," *IEEE Access*, vol. 7, pp. 49111–49124, 2019.

[9] Z. Wang, J. Zhou, J. Wang, W. Du, J. Wang, X. Han, and G. He, "A novel fault diagnosis method of gearbox based on maximum kurtosis spectral entropy deconvolution," *IEEE Access*, vol. 7, pp. 29520–29532, 2019, doi: 10.1109/ACCESS.2019.2900503.

[10] H. Guo, Q. Zhu, J. Tang, F. Nian, W. Liu, R. Zhao, F. Du, B. Yang, and J. Liu, "A temperature and humidity synchronization detection method based on microwave coupled-resonator," *Sens. Actuators B, Chem.*, vol. 261, pp. 434–440, May 2018.

[11] H. Huang, X. Chen, and J. Zhang, "Weight self-adjustment adams implicit filtering algorithm for attitude estimation applied to underwater gliders," *IEEE Access*, vol. 4, pp. 5695–5709, 2016.

[12] H. Cao, Y. Liu, Z. Kou, Y. Zhang, X. Shao, J. Gao, K. Huang, Y. Shi, J. Tang, C. Shen, and J. Liu, "Design, fabrication and experiment of double U-Beam MEMS vibration ring gyroscope," *Micromachines*, vol. 10, no. 3, p. 186, Mar. 2019.

[13] X. Ding, K. Zhu, and H. Li, "A switch-bridge-based readout circuit for differential capacitance measurement in MEMS resonators," *IEEE Sensors J.*, vol. 17, no. 21, pp. 6978–6985, Nov. 2017.

[14] H. Cao, H. Li, J. Liu, Y. Shi, J. Tang, and C. Shen, "An improved interface and noise analysis of a turning fork microgyroscope structure," *Mech. Syst. Signal Process.*, vols. 70–71, pp. 1209–1220, Mar. 2016.

[15] Q. Shen, H. Chang, Y. Wu, and J. Xie, "Turn-on bias behavior prediction for micromachined coriolis vibratory gyroscopes," *Measurement*, vol. 131, pp. 380–393, Jan. 2019.

[16] H. Cao, H. Li, X. Shao, Z. Liu, Z. Kou, Y. Shan, Y. Shi, C. Shen, and J. Liu, "Sensing mode coupling analysis for dual-mass MEMS gyroscope and bandwidth expansion within wide-temperature range," *Mech. Syst. Signal Process.*, vol. 98, pp. 448–464, Jan. 2018.

[17] H. Cao, Y. Zhang, Z. Han, X. Shao, J. Gao, K. Huang, Y. Shi, J. Tang, C. Shen, and J. Liu, "Pole-zero temperature compensation circuit design and experiment for dual-mass MEMS gyroscope bandwidth expansion," *IEEE/ASME Trans. Mechatronics*, vol. 24, no. 2, pp. 677–688, Apr. 2019, doi: 10.1109/TMECH.2019.2898098.

[18] S. A. Zotov, B. R. Simon, I. P. Prikhodko, A. A. Trusov, and A. M. Shkel, "Quality factor maximization through dynamic balancing of tuning fork resonator," *IEEE Sensors J.*, vol. 14, no. 8, pp. 2706–2714, Aug. 2014.

[19] C. Shen, Y. Zhang, J. Tang, H. Cao, and J. Liu, "Dual-optimization for a MEMS-INS/GPS system during GPS outages based on the cubature Kalman filter and neural networks," *Mech. Syst. Signal Process.*, vol. 133, Nov. 2019, Art. no. 106222.

[20] H. Cao, Y. Zhang, C. Shen, Y. Liu, and X. Wang, "Temperature energy influence compensation for MEMS vibration gyroscope based on RBF NN-GA-KF method," *Shock Vibrat.*, vol. 2018, pp. 1–10, Dec. 2018.

[21] C. Shen, Y. Zhang, X. Guo, X. Chen, H. Cao, J. Tang, J. Li, and J. Liu, "Seamless GPS/Inertial navigation system based on self-learning square-root cubature Kalman filter," *IEEE Trans. Ind. Electron.*, to be published, doi: 10.1109/TIE.2020.2967671.

[22] H. Cao, H. Li, Z. Kou, Y. Shi, J. Tang, Z. Ma, C. Shen, and J. Liu, "Optimization and experimentation of dual-mass MEMS gyroscope quadrature error correction methods," *Sensors*, vol. 16, no. 1, p. 71, Jan. 2016.

[23] B. Chaumet, B. Leverrier, C. Rougeot, and S. Bouyat, "A new silicon tuning fork gyroscope for aerospace applications," in *Proc. Symp. Gyro Technol.*, 2009, pp. 1.1–1.13.

[24] D. Maeda, K. Ono, J. Giner, M. Matsumoto, M. Kanamaru, T. Sekiguchi, and M. Hayashi, "MEMS gyroscope with less than 1-deg/h bias instability variation in temperature range from −40 °C to 125 °C," *IEEE Sensors J.*, vol. 18, no. 3, pp. 1006–1015, Feb. 2018.

[25] J. Su, D. Xiao, Z. Chen, Z. Hou, and X. Wu, "Dynamic force balancing for the sense mode of a silicon microgyroscope," *Meas. Sci. Technol.*, vol. 24, no. 9, Aug. 2013, Art. no. 095105.

[26] D. Xiao, J. Su, Z. Chen, Z. Hou, X. Wang, and X. Wu, "Improvement of mechanical performance for vibratory microgyroscope based on sense mode closed-loop control," *J. Micro/Nanolithography, MEMS, MOEMS*, vol. 12, no. 2, Apr. 2013, Art. no. 023001.

[27] C. He, Q. Zhao, Y. Liu, Z. Yang, and G. Yan, "Closed loop control design for the sense mode of micromachined vibratory gyroscopes," *Sci. China Technolog. Sci.*, vol. 56, no. 5, pp. 1112–1118, Apr. 2013.

[28] R. Wilcock and M. Kraft, "Genetic algorithm for the design of electro-mechanical sigma delta modulator MEMS sensors," *Sensors*, vol. 11, no. 10, pp. 9217–9232, Sep. 2011.

[29] F. Chen, H. Chang, W. Yuan, R. Wilcock, and M. Kraft, "Parameter optimization for a high-order band-pass continuous-time sigma-delta modulator MEMS gyroscope using a genetic algorithm approach," *J. Micromech. Microeng.*, vol. 22, no. 10, Aug. 2012, Art. no. 105006.

[30] Z. Hu and B. Gallacher, "A mode-matched force-rebalance control for a MEMS vibratory gyroscope," *Sens. Actuators A, Phys.*, vol. 273, pp. 1–11, Apr. 2018.

[31] C. D. Ezekwe and B. E. Boser, "A mode-matching $\sum \Delta$ closed-loop vibratory gyroscope readout interface with a 0.004 o/s/$\sqrt{}$Hz noise floor over a 50 Hz band," *IEEE J. Solid-State Circuits*, vol. 43, no. 12, pp. 3039–3048, Dec. 2008.

[32] F. Chen, W. Yuan, H. Chang, G. Yuan, J. Xie, and M. Kraft, "Design and implementation of an optimized double closed-loop control system for MEMS vibratory gyroscope," *IEEE Sensors J.*, vol. 14, no. 1, pp. 184–196, Jan. 2014.

[33] W.-T. Sung, S. Sung, J. G. Lee, and T. Kang, "Design and performance test of a MEMS vibratory gyroscope with a novel AGC force rebalance control," *J. Micromech. Microeng.*, vol. 17, no. 10, pp. 1939–1948, Aug. 2007.

[34] J. Cui, Z. Guo, Q. Zhao, Z. Yang, Y. Hao, and G. Yan, "Force rebalance controller synthesis for a micromachined vibratory gyroscope based on sensitivity margin specifications," *J. Microelectromech. Syst.*, vol. 20, no. 6, pp. 1382–1394, Dec. 2011.

[35] C. H. He, D. C. Liu, Q. C. Zhao, Y. F. En, Z. C. Yang, D. C. Zhang, and G. Z. Yan, "A novel narrow-band force rebalance control method for the sense mode of MEMS vibratory gyroscopes," *Measurement*, vol. 62, pp. 197–204, Feb. 2015.

[36] C. He, Q. Zhao, Q. Huang, L. Lin, Z. Yang, D. Zhang, and G. Yan, "A novel robust design method for the sense mode of a MEMS vibratory gyroscope based on fuzzy reliability and taguchi design," *Sci. China Technological Sci.*, vol. 60, no. 2, pp. 317–324, 2017.

HUILIANG CAO (Member, IEEE) received the Ph.D. degree in instrument science and technology from Southeast University, Nanjing, China, in 2014. From 2011 to 2012, he studied as a Research Ph.D. student with the School of Electrical and Computer Engineering, Georgia Institute of Technology, Atlanta, USA. He is currently a Postgraduate Tutor and an Associate Professor of the School of Instrument and Electronics, North University of China. He is one of the Top Young Academic Leaders of Higher Learning Institutions of Shanxi and Young Academic Leaders of the North University of China, Taiyuan, Shanxi, China. His research interest includes the areas of MEMS inertial devices.

RIHUI XUE received the B.S. degree from the North University of China, Taiyuan, Shanxi, China, in 2019, where he is currently pursuing the M.S. degree with the School of Instrument and Electronics. His research interest is in the fields of MEMS gyroscope circuit design.

QI CAI received the B.S. degree from the North University of China, Taiyuan, Shanxi, China, in 2018, where he is currently pursuing the M.S. degree with the School of Instrument and Electronics. His research interest is in the fields of MEMS sensor structure design.
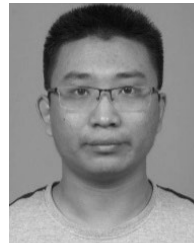
JINYANG GAO received the B.S. degree from the University of Electronic Science and Technology of China, Sichuan, China, in 2012, and the Ph.D. degree from Shanghai Jiao Tong University, Shanghai, China, in 2017. He is currently an Assistant Professor with the North University of China, Shanxi, China. His research interests include capsule robot, wireless power transmission and related electronic circuit design, and gastrointestinal biomechanics.

RUI ZHAO received the B.S. degree in microelectronics and the M.E. degree in micro-electronics and solid state electronics from the North University of China, Taiyuan, China, in 2009 and 2012, respectively, and the Ph.D. degree in microelectronics and solid state electronics from the Institute of Microelectronics, Peking University, Beijing, China, in 2016. He is currently working as a Junior Research Fellow with the Science and Technology on Electronic Test & Measurement Laboratory, School of Instrument and Electronics, and the Ministry of Education Key Laboratory Instrumentation Science & Dymanic Measurement, North University of China, Taiyuan. He is also working in the field of development of MEMS/NEMS bio/chemical sensors, the self-assembly of nanomaterials and the development of biosensor devices based on plasmonics. His current research interest includes design and fabrication of MEMS/NEMS/MOEMS inertial sensors.
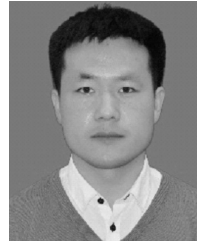
YUNBO SHI received the B.S. and M.S. degrees from the North University of China, Shanxi, China, in 1995 and 2003, respectively, and the Ph.D. degree from the Beijing Institute of Technology of China, in 2014. He is currently a Professor. His research interest is in the fields of measurement, semiconductor materials, and devices.

KUN HUANG received the B.S. and M.S. degrees from the North University of China, Shanxi, China, in 2008 and 2011, respectively, and the Ph.D. degree from Shanghai Jiao Tong University, in 2016. He has been working with the North University of China, since 2016. His research direction is the semiconductor micro–nano electromechanical device in the systems.

XINGLING SHAO received the M.S. degree in instrument science and technology from the North University of China, Shanxi, China, in 2012, and the Ph.D. degree in navigation, guidance and control from Beihang University, Beijing, China, in 2016. Since 2016, he has been with the Department of Instrument and Electronics, North University of China, Shanxi, as a Professor. His current research interests are in the fields of anti-disturbance control theory and application for nonlinear uncertain systems.

CHONG SHEN received the Ph.D. degree in instrument science and technology from Southeast University, Nanjing, China, in 2013. He is currently an Associate Professor of the School of Instrument and Electronics, North University of China, Taiyuan, Shanxi, China. His research interests include the areas of MEMS inertial devices de-noising and inertial guidance system design.

● ● ●